Chemical Physics Letters 681 (2017) 56–63

Contents lists available at ScienceDirect

Chemical Physics Letters

journal homepage: www.elsevier.com/locate/cplett

Research paper

Transition from metal-ligand bonding to halogen bonding involving a metal as halogen acceptor a study of Cu, Ag, Au, Pt, and Hg complexes

Vytor Oliveira *, Dieter Cremer

Computational and Theoretical Chemistry Group (CATCO), Department of Chemistry, Southern Methodist University, 3215 Daniel Ave, Dallas, TX 75275-0314, USA

ARTICLE INFO

Article history:
Received 8 January 2017
In final form 16 May 2017
Available online 20 May 2017

ABSTRACT

Utilizing all-electron Dirac-exact relativistic calculations with the Normalized Elimination of the Small Component (NESC) method and the local vibrational mode approach, the transition from metal-halide to metal halogen bonding is determined for Au-complexes interacting with halogen-donors. The local stretching force constants of the metal-halogen interactions reveal a smooth transition from weak non-covalent halogen bonding to non-classical 3-center-4-electron bonding and finally covalent metal-halide bonding. The strongest halogen bonds are found for dialkylaurates interacting with Cl_2 or FCl. Differing trends in the intrinsic halogen-metal bond strength, the binding energy, and the electrostatic potential are explained.

1. Introduction

Halogen bonding (XB) involves the interaction between a halogen donor molecule (YX) and a halogen acceptor molecule AR_n where A is an electron rich atom [1]. As in the case of hydrogen bonding, XB is a result of stabilizing covalent, electrostatic, inductive, and dispersion interactions, which are reduced by destabilizing exchange repulsion [1–3]. XB is of chemical relevance in catalysis, for the design of supramolecular structures, ion transport, and sensing [1]. There are numerous experimental and computational studies of the interactions between YX bonds and organic Lewis bases. However, XB has also been observed for transition metal complexes where the halogen accepting A is a metal M [1,4,5].

Koten and co-workers reported an organometallic complex in which a I_2 was coordinated to a metal center in a linear fashion (I-I-M close to 180) [6]. They suggested that the d_z^2 lone pair orbital of the metal would donate charge to the empty $\sigma^\star$(I-I) of I_2, which is typical of XB [6–9]. Cotton and co-workers [10] reported a complex were I_2 formed a bent interaction with a metal center. They suggested that the I_2 donates charge to the metal center in this case. Rogachev and Hoffmann [11] confirmed the $I_2\cdots M$ bond mechanism for planar Pt-complexes. These authors studied also metal-iodine complexes in which I_2 acts as an electron donor thus replacing XB by normal covalent metal-iodine bonding. They also investigated how the binding energy and bond distance between I_2 and the organometallic molecule is affected by having different types of metals (Co, Rh, Ir, Ni, Pd, Pt) and different ligands coordinated to the metal. Replacing Pt by Pd and then Ni leads to a weakening of XB.

An unusual octahedral cationic platinum complex with a neutral I_2 ligand coordinated to the metal in a end-on fashion was reported by Nagasawa and co-workers [12] Notable is the large I-I distance in several of these complexes [6–9,11,12], which may not be only due to the donation of the lone pair of the metal into the $\sigma^\star$(I-I) of iodine but may already indicate an advanced stage in the oxidative addition of I_2 where the metal is bound to I_2 by 3c-4e (3-center-4-electron) bonding or even due to an ion-pair $I^-\cdots$I-M^+ formation. Recently, Kukushkin and co-workers detected and studied theoretically the formation of XB and bifurcated XB between halocarbons and organoplatinum complexes [13] Zeng and co-workers [14] did second order perturbation theory (MP2) calculations and found that strong halogen bonds of covalent character are formed between interhalogens and Pt(II) in cis/trans-$Pt(NH_3)_2X2$ (X = OH, F, Cl, Br). Li and co-workers [15] carried out an MP2 investigation to study the formation of XB involving gold. Zhao studied the interaction between F_3CX (X = I, Br, Cl) and small gold clusters (Au_n n = 2, 3, 4) and found that X can act as an electron donor, forming a stronger interaction, or as a electron acceptor forming weak XBs [16]. Young and co-workers [17] reported the formation of $F_2\cdots$Hg when Hg is trapped in argon matrices doped with F_2 and suggested that the analogous interaction of heavier halogens could be important for understanding the environmental chemistry of Hg. Blakey and co-workers used different spectroscopic techniques (Synchrotron X-ray photoelectron

* Corresponding author.
E-mail addresses: voliveira@smu.edu (V. Oliveira), dcremer@smu.edu (D. Cremer).

http://dx.doi.org/10.1016/j.cplett.2017.05.045
0009-2614/

spectroscopy, UV–vis, surface enhanced Raman spectroscopy) and found evidence for the formation of XB involving iodoperfluorobenzenes and gold nanoparticles [18].

In the current work, the interactions between X-Y (dihalogens, interhalogens, and halohydrocarbons with X being Cl, Br, or I) and neutral or anionic metal complexes MR_n (M: Cu, Ag, Au, Pt, Hg) are quantum chemically investigated using an all-electron Dirac-exact scalar relativistic (spin free) method in combination with a rung 3 exchange-correlation functional. The strength of the metal-halogen bonding (XB-M) interactions will be quantified with the corresponding local stretching force constant [19–23]. The objectives of this work are to answer the following questions. (i) How strong are the interactions between Cu, Ag, Au ions and I_2 or CF_3I? (ii) What role do scalar relativistic effects play in this connection? (iii) How strong are covalent and/or electrostatic interactions between the metal complex and the X-donor? (iv) Can one tune the bonding mechanism between metal and iodine by varying the metal atom, possible ligands, or the halogen donor?

The computational methods used to answer these questions are described in the following section. Results and discussions are found in the third section of this work whereas the conclusions are given in the final section.

2. Computational methods

Molecular geometries and complex binding energies were computed utilizing the all-electron Dirac-exact Normalized Elimination of the Small Component (NESC) method [24] as developed and implemented by Zou, Filatov, and Cremer [25], which provides a more reliable account of energies, geometries, vibrational frequencies [26], and other response properties than the effective core potentials normally used [25–27]. NESC was used in connection with the rung 3 (meta-GGA) exchange correlation functional TPSS [28] that provides reliable data for transition metal complexes as has been documented in the literature [29,30]. TPSS was combined with the empirical dispersion correction D3 [31] and the Becke-Johnson damping parameters (BJ) [32] to accurately model dispersion interactions. Calculated binding energies were corrected for basis set superposition errors (BSSE) employing the counterpoise correction.[33].

As suitable relativistic basis sets, the segmented contracted Sapporo triple zeta basis sets Sapporo-DKH3-TZP-2012 [34] for Cu, Ag, Au, Hg, and I were chosen, whereas for all other atoms (Cl, C, H, F and N) the non-relativistic Sapporo-TZP-2012 basis sets[35,36] were used. Since 24 of the 29 complexes studied are anionic and highly polarizable, s-, p-, d-, f-, etc. sets of basis functions were augmented by one set of diffuse functions to better describe the electron density far from the nuclei. All DFT calculations were performed with tight convergence criteria (changes in the density matrix elements in the converged SCF (self-consistent field): $<10^{-10}$; changes in the forces of the optimized geometry: $<10^{-7}$ hartree/bohr) and an ultrafine grid [37].

For all molecules investigated, analytical vibrational frequencies in the harmonic approximation were calculated to (i) characterize each stationary point as minimum (or saddle point) and (ii) determine local vibrational modes and their properties according to the method developed by Konkoli and Cremer [19,38,20]. The Konkoli-Cremer modes are the local equivalent of the normal vibrational modes and their frequencies can be experimentally determined in special cases [38]. The local stretching force constants can be used to determine the intrinsic strength of a bond [22]. Furthermore, the description of the intrinsic bond strength via local stretching force constants can be simplified by using the latter to determine a bond strength order (BSO) [39].

According to the generalized Badger rule [40,39], BSO values $n(XB)$ of the XB are related to the calculated $k^a(XB)$ values via a power relationship [40,22]

$$n = a(k^a)^b \quad (1)$$

where constants $a = 0.696$ and $b = 0.660$ define for the I-I bond in I_2 a BSO value $n = 1.00$ and for the corresponding 3c-4e bond in $[I\cdots I\cdots I]^- n = 0.50$. According to the Rundle-Pimentel model of bonding, the $[I\cdots I\cdots I]^-$ anion has 2e in a bonding and 2e in a non-bonding orbital, which suggests a non-classical (NC) BSO (I···I) value being half of that of the di-iodine bond. Eq. (1) also implies that for $k^a = 0$, an n value of zero results.

Since NC 3c-4e bonding can play an important role in XB [2], its magnitude was assessed in percentage using the ratio $n(X\cdots A/n(XY)) \times 100$. If the ratio of bond strengths leads to unity, 3c-4e bonding is fulfilled by 100% as in the $[I\cdots I\cdots I]^-$ anion. Values below 75% indicate that 3c-4e bonding plays a minor role. Values above 100% indicate the formation of inverted 3c-4e bonding (i-NC): The XA interactions are stronger than the XY interactions. Values above 100% are listed in the tables to quickly identify inverted 3c-4e bonding, but can be compared with other values via their reciprocal $(n(Y\cdots X/n(XA)) \times 100)$.

Local properties of the electron density distribution, $\rho(\mathbf{r})$, and energy density distribution, $H(\mathbf{r})$, were also computed at the NESC/TPSSD3 level of theory and used to determine the covalent character of the XY and XA interactions with the help of the Cremer-Kraka criteria for covalent bonding [41,42]. According to these criteria a negative and therefore stabilizing energy density at the bond critical point $\mathbf{r}_b$ ($H(\mathbf{r}_b) = H_b < 0$) indicates a dominating covalent character, whereas a positive (destabilizing) energy density ($H_b > 0$) is associated with predominant electrostatic interactions.

Using the natural bond orbital (NBO) method of Weinhold and co-workers [43], NBO atomic charges were calculated and used to assess the charge transfer between the monomers of an XB-M complex.

The electrostatic character of the interactions was investigated by using the extremal value V_{ext} of the electrostatic potential $V(\mathbf{r})$ on the van der Waals surface (modeled by the 0.001 e/Bohr^3 electron density surface) of the halogen donor monomers (i.e. V_{ext} is a maximum). The halogen acceptor ability of a monomer AR_n was assessed by determining the minimum value V_{ext} in the lp(A) region. $V(\mathbf{r})$ (measured in eV) is positive in the case of a σ-hole of a halogen and negative in the lp-region of a hetero atom.

The calculation of the NESC energies, geometries and frequencies as well as the local mode properties was performed with the program COLOGNE2016 [44]. For the NBO analysis, the program NBO6 [45] was used. The local properties of the electron density distribution, $\rho(\mathbf{r})$, and energy density distribution, $H(\mathbf{r})$ at the bond critical point (see Supporting Information (SI)) and the electrostatic potential at the van der Waals surface (0.001 e/bohr^3: e: electron) were analyzed with the Multiwfn program [46]. DFT calculations were performed with the package Gaussian09 [47].

3. Results and discussion

Fig. 1 summarizes for complexes (**1**–**29**) selected bond distances and bond angles. NESC/TPSS-D3 binding energies ΔE and charge transfer (CT) values are listed in Table 1 for **1**–**29** where also the XA and XY interaction distances r, local stretching force constants k^a, local stretching frequencies ω^a, and BSO values n are compared. Also given is the percentage of 3c-4e character that is used to distinguish between NC and XB-M bonding (see Fig. 2). In Table 2, X-donor properties such as r, k^a, n, and ω^a for the XY bond are listed for **30**-**42**. Also given is the extremal value V_{ext} in the van der Waals

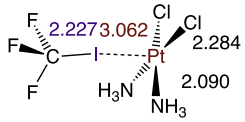

C-I-Pt = 172.0 I-Pt-Cl = 99.0
I-Pt-N = 82.2 N-Pt-Cl = 178.2

1, C_s

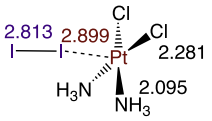

I-I-Pt = 173.8 I-Pt-Cl = 99.7
I-Pt-N = 82.7 N-Pt-Cl = 177.3

2, C_s

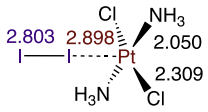

I-I-Pt = 180.0 I-Pt-Cl = 93.6
I-Pt-N = 89.4 N-Pt-Cl = 90.0

3, C_{2v}

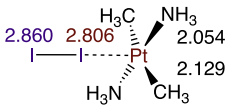

I-I-Pt = 180.0 I-Pt-C = 92.4
I-Pt-N = 88.9 C-Pt-N = 90.0

4, C_2

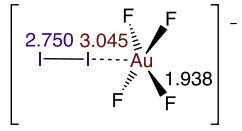

I-I-Au = 180.0 F-Au-F = 178.3
I-Au-F = 90.8

5, C_{4v}

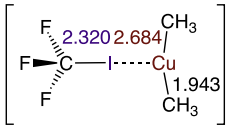

C-I-Cu = 180.0 I-Cu-C = 93.8
C-Cu-C =172.5

6, C_s

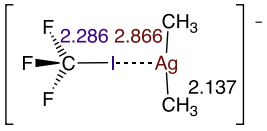

C-I-Ag = 180.0 I-Ag-C = 91.1
C-Ag-C =177.7

7, C_s

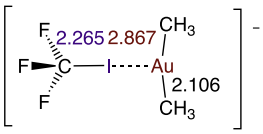

C-I-Au = 180.0 I-Au-C = 91.5
C-Au-C =177.1

8, C_s

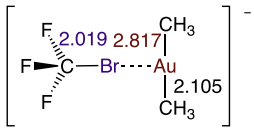

C-Br-Au = 180.0 Br-Au-C = 90.9
C-Au-C = 178.2

9, C_s

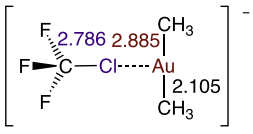

C-Cl-Au = 180.0 Cl-Au-C = 90.3
C-Au-C = 179.3

10, C_s

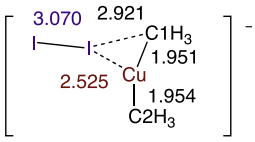

I-I-Cu = 161.0 C1-Cu-C2 = 158.4
I-Cu-C1 = 80.4 I-Cu-C2 = 121.2

11, C_s

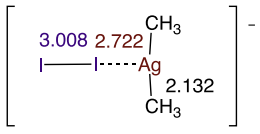

I-I-Ag = 180.0 I-Ag-C = 92.2
C-Ag-C =175.7

12, C_{2v}

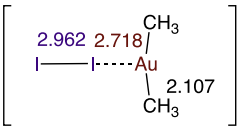

I-I-Au = 180.0 I-Au-C = 92.3
C-Au-C =175.4

13, C_{2v}

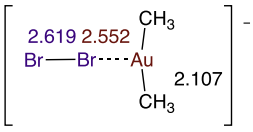

Br-Br-Au = 180.0 Br-Au-C = 92.1
C-Au-C = 175.8

14, C_{2v}

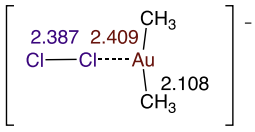

Cl-Cl-Au = 180.0 Cl-Au-C = 92.1
C-Au-C = 175.8

15, C_{2v}

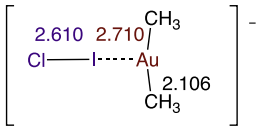

Cl-I-Au = 180.0 I-Au-C = 92.2
C-Au-C = 175.6

16, C_{2v}

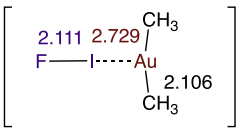

F-I-Au = 180.0 I-Au-C = 92.0
C-Au-C = 175.9

17, C_{2v}

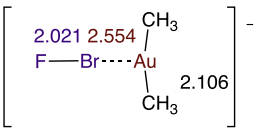

F-Br-Au = 180.0 Br-Au-C = 91.9
C-Au-C = 176.3

18, C_{2v}

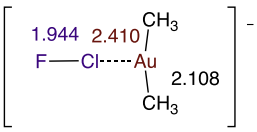

F-Cl-Au = 180.0 Cl-Au-C = 91.9
C-Au-C = 176.2

19, C_{2v}

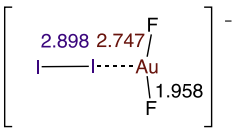

I-I-Au = 180.0 I-Au-F = 92.9
F-Au-F =174.2

20, C_{2v}

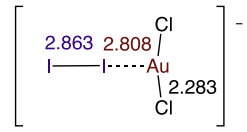

I-I-Au = 180.0 I-Au-Cl = 94.0
Cl-Au-Cl =171.9

21, C_{2v}

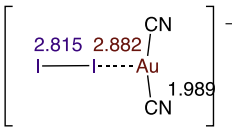

I-I-Au = 180.0 I-Au-C = 92.3
C-Au-C = 175.4

22, C_{2v}

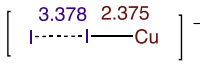

I-I-Cu = 180.0

23, $C_{\infty v}$

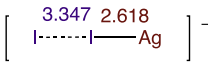

I-I-Ag = 180.0

24, $C_{\infty v}$

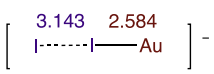

I-I-Au = 180.0

25, $C_{\infty v}$

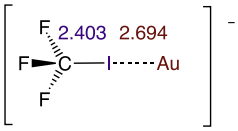

C-I-Au = 180.0

26, C_{3v}

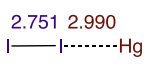

I-I-Hg = 180.0

27, $C_{\infty v}$

I-I-I = 180.0

28, $D_{\infty h}$

Au-I-Au = 180.0

29, $D_{\infty h}$

Fig. 1. Schematic presentation of the geometries of complexes **1**–**29**. Selected XM distances are shown in red and XY distances in blue. Distances in Å and angles in degrees. NESC/TPSS calculations.

Table 1
Summary of energy, geometry, and vibrational data of all complexes investigated.[a].

#	Complex (Symmetry)	ΔE	CT	r (XA)	r (XY)	k^a (XA)	k^a (XY)	ω^a (XA)	ω^a (XY)	n (XA)	n (XY)	3c-4e %	Type
1	$F_3Cl\cdots Pt(NH_3)_2Cl_2$ *cis*(C_s)	12.0	0.152	3.062	2.227	0.134	1.289	54	447	0.185	0.823	22	XB-M
2	$I_2\cdots Pt(NH_3)_2Cl_2$ *cis*(C_s)	17.9	0.288	2.899	2.813	0.496	1.016	105	165	0.438	0.703	62	XB-M
3	$I_2\cdots Pt(NH_3)_2Cl_2$ *trans*(C_{2v})	14.5	0.276	2.898	2.803	0.501	1.042	105	167	0.441	0.715	62	XB-M
4	$I_2\cdots Pt(NH_3)_2(CH_3)_2$ *trans*	27.7	0.357	2.806	2.860	0.699	0.906	124	156	0.549	0.652	84	NC
5	$I_2\cdots AuF_4^-$ (C_{4v})	9.9	0.175	3.045	2.750	0.255	1.207	75	180	0.282	0.788	36	XB-M
6	$F_3Cl\cdots Cu(CH_3)_2^-$ (C_s)	27.5	0.380	2.684	2.320	0.467	0.883	137	370	0.421	0.641	66	XB-M
7	$F_3Cl\cdots Ag(CH_3)_2^-$ (C_s)	23.2	0.328	2.866	2.286	0.432	0.992	112	392	0.400	0.692	58	XB-M
8	$F_3Cl\cdots Au(CH_3)_2^-$ (C_s)	23.9	0.297	2.867	2.265	0.472	1.116	102	416	0.424	0.748	57	XB-M
9	$F_3CBr\cdots Au(CH_3)_2^-$ (C_s)	15.3	0.233	2.817	2.019	0.355	1.281	103	457	0.351	0.819	43	XB-M
10	$F_3CCl\cdots Au(CH_3)_2^-$ (C_s)	9.4	0.135	2.885	1.786	0.181	1.921	102	604	0.225	1.071	21	XB-M
11	$I_2\cdots Cu(CH_3)_2^-$ (C_s)	46.8	0.659	2.525	3.070	0.715	0.421	170	106	0.558	0.393	142	i-XB-M
12	$I_2\cdots Ag(CH_3)_2^-$ (C_{2v})	40.3	0.613	2.722	3.008	0.733	0.533	146	119	0.567	0.459	124	i-NC
13	$I_2\cdots Au(CH_3)_2^-$ (C_{2v})	38.8	0.522	2.718	2.962	0.842	0.631	136	130	0.621	0.514	121	i-NC
14	$Br_2\cdots Au(CH_3)_2^-$	38.3	0.585	2.552	2.619	0.908	0.690	165	172	0.653	0.545	120	i-NC
15	$Cl_2\cdots Au(CH_3)_2^-$ (C_{2v})	34.4	0.636	2.409	2.387	0.998	0.645	239	250	0.695	0.521	133	i-XB-M
16	$ClI\cdots Au(CH_3)_2^-$ (C_{2v})	41.9	0.507	2.710	2.610	0.885	0.816	139	225	0.642	0.608	106	i-NC
17	$FI\cdots Au(CH_3)_2^-$	43.1	0.449	2.729	2.111	0.857	1.438	137	384	0.629	0.884	71	NC
18	$FBr\cdots Au(CH_3)_2^-$	42.5	0.522	2.554	2.021	0.947	1.280	169	377	0.671	0.819	82	NC
19	$FCl\cdots Au(CH_3)_2^-$	39.7	0.582	2.410	1.944	1.034	1.074	243	385	0.711	0.729	98	NC
20	$I_2\cdots AuF_2^-$ (C_{2v})	29.9	0.452	2.747	2.898	0.694	0.769	124	143	0.547	0.585	94	NC
21	$I_2\cdots AuCl_2^-$ (C_{2v})	23.7	0.383	2.808	2.863	0.552	0.825	110	149	0.470	0.613	77	NC
22	$I_2\cdots Au(CN)_2^-$	17.3	0.282	2.882	2.815	0.454	0.970	100	161	0.413	0.682	61	XB-M
23	$CuI\cdots I^-$ ($C_{\infty v}$)	9.5 (79.3)[b]	0.315	3.378	2.375	0.219	1.367	77	235	0.255	0.855	30	XB
24	$AgI\cdots I^-$ ($C_{\infty v}$)	9.2 (69.7)[b]	0.341	3.347	2.618	0.228	0.972	78	169	0.262	0.683	38	XB
25	$AuI\cdots I^-$ ($C_{\infty v}$)	23.1 (61.2)[b]	0.437	3.143	2.584	0.393	1.203	163	163	0.376	0.786	48	XB
26	$F_3Cl\cdots Au^-$ (C_{3v})	35.8	0.297	2.694	2.403	0.703	0.605	124	306	0.551	0.499	110	i-NC
27	$I_2\cdots Hg$ ($C_{\infty v}$)	6.4	0.207	2.990	2.751	0.248	1.168	73	177	0.277	0.771	36	XB-M
28	$AuI\cdots Au^-$ ($D_{\infty h}$)	40.9	0.713	2.666	2.666	0.819	0.819	134	134	0.610	0.610	100	NC
29	$I_2\cdots I^-$ ($D_{\infty h}$)	37.9	0.559	2.968	2.968	0.606	0.606	127	127	0.500	0.500	100	NC

[a] Computed at NESC/TPSS-D3(BJ)/sapporo-DKH3-TZP-2012 for I, Au, Ag, Cu and-TZP-2012 for C, F and H. All atom basis sets are augmented by one set of diffuse functions per angular momentum. Binding energy ΔE in kcal/mol, halogen-acceptor r(XA) and halogen-donor r(XY) distances in Å, local XA and XY stretching force constant in mdyn/Å, local stretching frequency ω^a in cm^{-1}, bond strength order *n*, and Y-X-A 3c-4e bond % character given by $n(XA)/n(XY) \times 100$. XB-M: halogen bonding involving metal M; NC: nonclassical 3c-4e bonding; i-XB-M: inverse XB-M, i.e. $Y^- \cdots X - MR_2$; i-NC: inverse NC, i.e. BSO(X···M) > BSO(X···Y)

[b] Numbers in parentheses refer to the $M\cdots I$ bond dissociation energy.

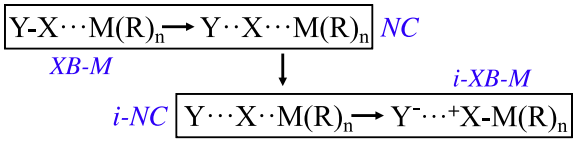

Fig. 2. Schematic presentation of the conversion of an XB-M interaction into a 3c-4e-bonding situation where either the XY interaction (NC: non-classical bonding) or the XM interaction (i-NC: inverted non-classical bonding) being somewhat stronger. The latter can convert into a covalent XM bond and interact with a negatively charged Y via i-XB-M (inverted XB-M).

surface of X. For X-acceptors **43**-**57**, just V_{ext} is given in Table 2. In Fig. 3, the BSO values of the various XB-M are compared. XB-M interactions can adopt BSO values from 0.2 to 0.8 where the lower values (<0.5) indicate weak and normal XB-M whereas values of 0.5 and larger give the transition from NC to i-NC and i-XB-M bonding. All XB-M turn out to have more or less covalent character ($H_b < 0$; see SI).

In the following, we will discuss the interactions of X-donors with (i) planar transition metal complexes (TMC) leading to pyramidal interaction complexes, (ii) linear TMC leading to T-structures, and (iii) TM leading to linear structures.

Halogen bonding involving square planar TMC. TMC **1** is stabilized by a XB-M between F_3CI and cis-$Pt(NH_3)_2Cl_2$. The binding energy ΔE is only 12 kcal/mol and the BSO value 0.185. F_3CI is a too weak X-donor to establish a stronger XB-M. This is also reflected by comparing the σ-holes of the X-donors, which increase in the series F_3C-Cl (V_{ext}: 0.86 eV) < F_3C-Br (1.05) < Cl-Cl (1.11) < F_3C-I (1.27) < Br-Br (1.28) < I-I (1.31) < Cl-I (1.83; Table 2).

A relatively strong XB-M is obtained by using I-I where *n* is 0.438 for cis-platin while a slightly larger value of 0.441 results for trans-platin. An identical amount of 3c-4e character is calculated for **2** and **3** (62%), i.e. the charge transferred from a d_z^2(Pt) lone pair into the $\sigma^\star(I-I)$ orbital weakens (lengthens) the I-I bond and strengthens (shortens) the Pt···I interaction. The ΔE value (cis: 17.9; trans: 14.5 kcal/mol) is influenced by both the XB-M and the mutual polarizability of the monomers, which is larger for cis-platin and can be enhanced by a slight tilting of the plane of cis-platin relative to the I-I bond axis (Fig. 1). In this way the positively charged H atoms of the NH_3 ligands can better interact with the π-density of the negatively charged I atom next to Pt.

The strength of the XB-M interactions can be increased by replacing the Cl ligands by electron donor ligands such as methyl (**4**): ΔE raises to 27.7 kcal/mol. This is parallel to an increase of the calculated CT to 0.357 e (Table 1; TMC **1**: 0.152; **3**: 0.276; **2**: 0.288 e). The larger CT causes a stronger Pt···I interaction (BSO: 0.549) and a weakening of the I-I bond (0.652) so that a delocalized 3c-4e system with 84% 3c-4e character and NC bonding results. Electron-withdrawing ligands in the TMC have the opposite effect as is documented by the low ΔE of $I_2\cdots AuF_4^-$ (**5**) (9.9 kcal/mol; CT: 0.175 e, BSO: 0.282).

Halogen bonding leading to T-structures. The anionic dimethylcuprate, dimethylargentate, and dimethylaurate (M: Cu, Ag, Au) are stronger electron donors and therefore their complexes with F_3C-I, **6**, **7**, and **8**, have BSO values of 0.421, 0.400, and 0.424, respectively (Table 1). It is remarkable that a similar trend is obtained for the electrostatic potential V_{ext} in the d-electron region of monomers MMe_2^- (Cu: −4.83, Ag: −4.65, Au: −4.88 eV, Fig. 4), which suggests that there is first a decrease in the polarization of

Table 2
Geometry, vibrational data, and values of the electrostatic potential for halogen donors and acceptors.[a]

#	X-Donor	r	k^a	n	ω^a	V_{ext}(X)	#	X-Acceptors	V_{ext}(A)
30	I-I	2.679	1.732	1.000	215	1.31	**43**	$Cu(CH_3)_2^-$	−4.83
31	Br-Br	2.305	2.298	1.205	314	1.28	**44**	$Ag(CH_3)_2^-$	−4.65
32	Cl-Cl	2.009	2.981	1.431	538	1.11	**45**	$Au(CH_3)_2^-$	−4.88
33	Cl-I	2.336	2.310	1.209	378	1.83	**46**	AuF_2^-	−4.63
34	F-I	1.931	3.492	1.589	599	2.32	**47**	$AuCl_2^-$	−4.21
35	F-Br	1.786	3.754	1.666	645	2.14	**48**	AuF_4^-	−3.76
36	F-Cl	1.655	4.135	1.776	755	1.73	**49**	$Au(CN)_2^-$	−3.71
37	F_3C-I	2.168	1.828	1.036	532	1.27	**50**	Hg	0.16
38	F_3C-Br	1.949	2.190	1.167	597	1.05	**51**	I^-	−5.28
39	F_3C-Cl	1.773	2.665	1.329	712	0.86	**52**	Cu^-	−5.06
40	Cu-I	2.326	1.791	1.022	269	−0.04	**53**	Ag^-	−4.91
41	Ag-I	2.560	1.354	0.850	199	−0.25	**54**	Au^-	−5.35
42	Au-I	2.488	1.966	1.087	208	0.53	**55**	$Pt(NH_3)_2Cl_2$ *cis*	−0.65
							56	$Pt(NH_3)_2Cl_2$ *trans*	−0.51
							57	$Pt(NH_3)_2(CH3)_2$ *trans*	−0.92

[a] Halogen-donor r(XY) distances in Å, XY stretching force constant in mdyn/Å, local stretching frequency ω^a in cm^{-1}. Since the I-I bond is chosen as a reference (n = 1.00), the BSO values n of other dihalogens are significantly stronger whereas M-I bonds are comparable in strength or weaker. Electrostatic potential at the σ-hole region of the X-donors V_{ext}(X) and at the lp region of X-acceptors V_{ext}(A) in eV. Computed at the 0.001 e/$Bohr^3$ electron density surface using NESC/TPSS-D3(BJ)/sapporo-DKH3-TZP-2012 method.

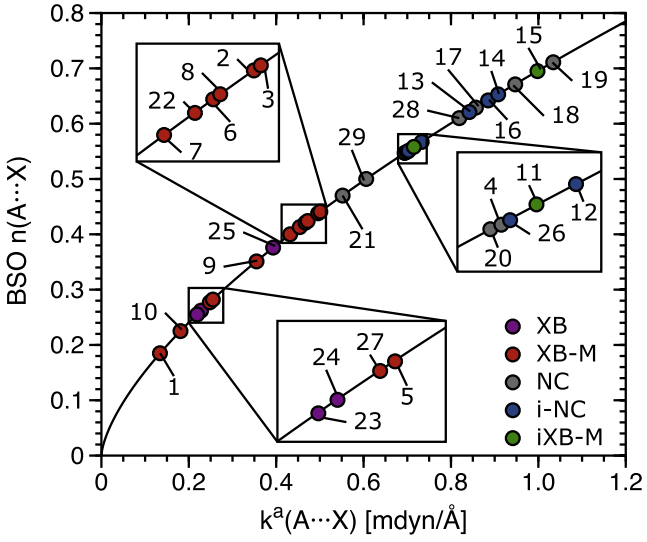

Fig. 3. Bond strength orders (BSO) n of the halogen bond XB-M given as a function of the local XB stretching force constant. For numbering of complexes, see Fig. 1. Green dots: XB-M; blue dots: NC and i-NC; red dots: i-XB bonding mechanisms. NESC/TPSS calculations. (For interpretation of the references to color in this figure legend, the reader is referred to the web version of this article.)

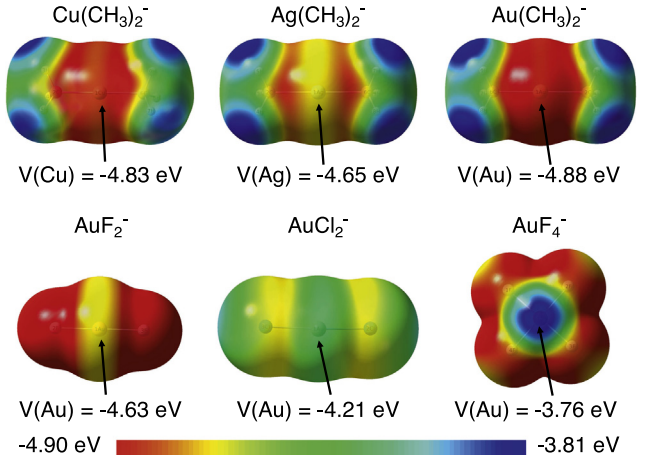

Fig. 4. Perspective drawings of the electrostatic potential V of some anionic halogen acceptors in eV, computed for the 0.001 e/$Bohr^3$ electron density surface. NESC/TPSS calculations.

the electron density when moving from XB-M complex **6** to **7** and then an increase again for **8**. The decrease in the polarization results from the higher electronegativity of Ag compared to Cu (Pauling scale: χ(M) = 1.90 (Cu); 1.93 (Ag); 2.54 (Au) [48]), which is confirmed by the trend in the positive metal NBO charges of the anions (0.413, 0.336, 0.213 e). The increase of the BSO value for **8** is a result of scalar relativistic effects, which lead to a contraction of the 6s orbital, but to an expansion of the 5d-orbitals where the latter are important for XB-M (see SI). The 5d-expansion facilitates the polarization of the dimethylaurate anion density as caused by F_3C-I thus leading to a BSO value of 0.424. The ΔE values decrease from 27.5 to 23.2 and 23.9 kcal/mol where the stability of **6** is a result of charge transfer/polarization (CT: 0.380, 0.328, 0.297 e; reduction in the length of the C-I bond: 2.320, 2.286, 2.265 relative to 2.168 Å), and the electrostatic attraction of positively charged methyl H atoms and the π(I) density (distance H,I: 3.471, 3.620, 3.611 Å; charge of closest H: 0.179, 0.174, 0.175 e). The polarizing power of F_3C-Br or F_3C-Cl is no longer sufficient ($\sigma(Br)$-hole in F_3C-Br: V_{ext} = 1.05; F_3C-Cl: 0.86; F_3C-I: 1.27 eV; Table 2) to form a strong complex: **9**: ΔE:15.3 kcal/mol, BSO: 0.351; 9.4, 0.225; Table 1). In the series **8**, **9**, **10**, ΔE, CT, V_{ext}, and BSO change in an adequate way indicating that XB-M dominates the complex stability.

The complexes so far discussed follow simple trends: The CT determines the strength of the XB-M (BSO value) and by this the ΔE value. This changes for the complexes formed between a di- or interhalogen and a dimethylmetal anionic X-acceptor $M(CH_3)_2^-$ (M = Cu, Ag, Au). In the series **11**, **12**, **13**, the M···I_2 interactions increase from Cu to Au (BSO: 0.558, 0.567, 0.621; Table 1), which surprisingly is parallel to an increase in the strength of the I-I bond (n: 0.393, 0.459, 0.514) caused by a reduced charge transfer (0.659, 0.613, 0.522 e, see Table 1). The strength of XB-M changes opposite to the change in ΔE: 46.8, 40.3, 38.8 kcal/mol (Table 1), which indicates that other factors than XB-M dominate the complex stability. The reason for this becomes obvious when investigating the T-structure of the Cu complex **11**: This is unstable because of a pseudo-Jahn–Teller effect. The first excited state, $^1A'$ can interact with the $^1A_1$ ground state via a a'-symmetrical vibration, which leads to distortion of the C_{2v}-symmetrical structure (Fig. 1) and converts XB-M into a interaction of I with both Cu and one of the

methyl groups. For **12** and **13**, the symmetrical T-structure remains. The favorable electrostatic potentials for M and X (Ag: −4.65; Au: −4.88; I: 1.31 eV, Table 2) seem to strengthen XB-M whereas CT and the electrostatic interactions with the methyl groups dominate the overall stability. In this connection the 3c4e interactions (Cu: 142; Ag: 124; Au: 121%) also favor the interaction between I and Au or Ag.

In general, the electrostatic potential has to be used with care [49] when explaining different trends between ΔE and BSO. Depending on the TMC geometry, it helps to understand the complex binding energy, but often V_{ext} fails to be useful for the analysis of the BSO values. This is quite obvious for the series of dihalogens I_2, Br_2, Cl_2 or interhalogens FCl, FBr, FI interacting with dimethylaurate (**13**-**15** and **17**-**19**, respectively). ΔE values decrease in line with V_{ext} of X whereas BSO and CT values increase (Table 1). Again, these are cases for which the intrinsic XB-M strength does not dominate the binding energy. The latter is strongly influenced by the strength of the XY bond, which, due to CT, weakens (e.g., for FCl, FBr, FI by 59, 51, 44% according to calculated BSO values; Table 1) and thereby reduces ΔE. The CT is directly related to the electronegativity χ of X: The larger $\chi(X)$ is the lower is the $\sigma^{\star}(XY)$ orbital and the stronger the CT.

In the series **13**-**15** and **17**-**19**, the XB-M is dominated by the electrostatic attraction between atoms Au and X (see SI), which is largest for the more electronegative Cl. The potential V_{ext} reflects the overall electrostatic interactions and therefore can only be related in a qualitative way to the TMC stability rather than the intrinsic strength of XB-M. Only if the latter is BSO-dominated, V_{ext} might be used to rationalize trends in the BSO. Hence, by comparing changes in ΔE and BSO values, different electronic effects determining the stability of the TMC can be distinguished (see SI).

If CT is the major reason for the XB-M strength, it gives insight into the covalent part of XB-M bonding, but there are also electrostatic, exchange repulsion, and dispersion interactions between X and M (see SI). None of the currently available methods including SAPT (Symmetry-Adapted Perturbation Theory [50]) can single out any of these interactions between the two atoms X and M, which is the reason why here only indirect information on these effects can be provided.

Forming a metal lone pair orbital of high density. In linear $[MY_2]^-$ with Y being a halogen or another ligand with π-electrons, bonding and antibonding $p\pi(Y) - d\pi(M) - p\pi(Y)$-orbitals are doubly occupied. For the bonding orbital, the Y-coefficient is large if the electronegativity of Y is large. Then, the orthogonal antibonding orbital has a large M-coefficient, i.e. antibonding $p\pi(Y) - d\pi(M) - p\pi(Y)$-orbital gets some lone-pair character (see orbital pictures in SI). This effect is enhanced for a relativistic M because of the well-known scalar relativistic expansion of the d-orbitals (see SI). V_{ext} values of AuF_2^- (-4.63), $AuCl_2^-$ (-4.21), and $Au(CN)_2^-$ (-3.71; Table 2) confirm this effect. Hence, AuF_2^- is better suited than $AuCl_2^-$ or $Au(CN)_2^-$ to bind I_2, which is in line with the ΔE (29.9, 23.7, 17.3 kcal/mol), CT (0.452, 0.383, 0.282 e), BSO (0.547, 0.470, 0.413) and 3c-4e values (94, 77, 61%). In these cases, the binding energy is dominated by the $M\cdots X$-interaction and makes it possible to fine-tune XB-M via the M,X-electronegativity difference in an easy to predict way.

Metal-halogen bonding leading to linear TMC. Despite the fact that the Hg atom has a $6s^2$-electron configuration and a relatively small positive electrostatic potential (V_{ext}(Hg): 0.16 eV), it can still be polarized by I_2 (ΔE = 6.4 kcal/mol) resulting in a weak XB-M (n = 0.277) for **27**. For Br_2 and Cl_2, smaller ΔE are obtained whereas FI leads to a ΔE of 10.8 kcal/mol. Attempts to find stable $HgF_2\cdots X_2$ or XY complexes led to unstable structures. Bare metal anions such as Cu^-, Ag^- and Au^- have a strongly negative electrostatic potential due to the extra electron ($V_{ext}(Cu^-)$: −5.06 eV; $V_{ext}(Ag^-)$: −4.91; $V_{ext}(Au^-)$: −5.35 eV). There is a strong charge transfer from the metal to the $\sigma^{\star}(XY)$-orbital so that a covalent M-I bond is formed, and the I-I bond dissolves: An $MI\cdots I^-$ complex results, which is characterized as i-XB-M bonding.

To confirm that no local minimum structure with a normal XB-M bond exists, a relaxed scan for the $I_2\cdots Au^-$ distance was carried out in the range 2.584 to 4.784 Å using increments of 0.2 Å. A single-well potential was found, which confirmed that an XB-M structure of the type I-I···Au does not exist. The strongest $MI\cdots I^-$ interactions are found for M = Au (BSO: 0.376, ΔE: 23.1 kcal/mol; Table 1, Cu: BSO: 0.255, ΔE: 9.5; Ag: BSO: 0.262, ΔE: 9.2). The stronger XB in $AuI\cdots I^-$ is due to the larger electrophilic character of Au, (NBO values for Au, Cu, Ag: −0.166, 0.139, 0.126 e) resulting in the formation of a positive electrostatic potential at the σ-hole of I (V_{ext}(I) = 0.53 eV) whereas negative V_{ext} values at I are obtained for CuI and AgI (V_{ext}(I): −0.04 and −0.25 eV; Table 2).

Replacing the terminal iodine atoms by Au leads to TMC **28**, which because of the relativistic d-expansion, has stronger 3c-4e bonds than I_3^- (n = 0.610 for **28**) and a larger ΔE (40.9 kcal/mol compared to 37.9 kcal/mol for **29**, Table 1).

4. Conclusions

In this work, we have for the first time determined the intrinsic XB-M strength by singling it out from the manifold of monomer–monomer interactions with the help of local XB-M stretching force constants and associated BSO values where we used Dirac-exact NESC calculations to reliably determine scalar relativistic effects for second order response properties. We note that this approach is based on features of the potential energy surface and its results can be directly verified with the help of vibrational spectroscopy. Hence, it can obtain atom,atom interactions, which are not accessible by SAPT or any other energy decomposition methods. Using this advantage and those of NESC the following results were obtained:

(1) XB-M bonding has chameleon-character as small electronic effects lead to a change in its nature, which varies from M, X-interactions typical of a heteroatom to non-classical 3c-4e bonding and, finally, the formation of an M-X ligand bond. The approach used in this work for the first time quantitatively reveals these changes via the BSO values, which are based on measurable quantities.
(2) XB-M can be found for planar and linear TMC of Au and Pt. For negatively charged atoms, a strong interaction with dihalogens results.
(3) XB-M involving derivatives of halotrifluoromethanes is weak or modestly strong. The BSO values are in line with the ΔE values (*XB-M-dominated TMCs*) and can be related to CT and V_{ext} values.
(4) In general, V_{ext} does not correlate with the BSO of XB-M. There is only a qualitative relationship with the binding energy. Similarly, the CT relates with ΔE, but not always with the BSO values of XB-M.
(5) Gold is a candidate for strong XB-M interactions due to its d-lone pair orbitals, which are easily accessible because of their scalar relativistic expansion and the negative charge of an aurate. If the latter has two strongly electronegative ligands with π-electron lone pairs (e.g., F), the availability of the Au lone pair is increased and XB-M strengthened as shown in this work.
(6) Interactions of aurates with XX or XY (X,Y: halogen) are no longer XB-M-dominated as the mutual polarization of the monomers determines the relatively high TMC stability whereas XB-M is best described as 3c4e-nonclassical

bonding that can vary strongly: the strongest XB-M bond is found for FCl rather than FI. Similarly, Cl_2 establishes a stronger XB-M than I_2 where the reason is the larger electronegativity of Cl that makes it possible that covalent contributions are supported by electrostatic attraction between Au and Cl.

Future work will focus on the "lone pair activation effect" in planar TMCs by using beside methyl also F ligands where the relativistic metals Pt and Au are first candidates. The planar TMCs are interesting as by front- and backside XB-M interactions long strands of TMCs with X-donors as di-iodo-acetylene or 1,4-diiodobenzene can be formed.

Acknowledgement

This work was financially supported by the National Science Foundation, Grant CHE 1464906. We thank SMU for providing computational resources. VO acknowledges financial support by CAPES (Brazil; fellowship grant BEX 9534-13-0).

Appendix A. Supplementary material

Supplementary data associated with this article can be found, in the online version, at http://dx.doi.org/10.1016/j.cplett.2017.05.045.

References

[1] G. Cavallo, P. Metrangolo, R. Milani, T. Pilati, A. Priimagi, G. Resnati, G. Terraneo, The halogen bond, Chem. Rev. 116 (4) (2016) 2478–2601.
[2] V. Oliveira, E. Kraka, D. Cremer, The intrinsic strength of the halogen bond: electrostatic and covalent contributions described by coupled cluster theory, Phys. Chem. Chem. Phys. 18 (2016) 33031–33046.
[3] V. Oliveira, E. Kraka, D. Cremer, Quantitative assessment of halogen bonding utilizing vibrational spectroscopy, Inorg. Chem. 56 (1) (2016) 488–502.
[4] L. Brammer, G. Minguez Espallargas, S. Libri, Combining metals with halogen bonds, CrystEngComm. 10 (2008) 1712–1727.
[5] R. Bertani, P. Sgarbossa, A. Venzo, F. Lelj, M. Amati, G. Resnati, T. Pilati, P. Metrangolo, G. Terraneo, Halogen bonding in metal-organic-supramolecular networks, Coord. Chem. Rev. 254 (5–6) (2010) 677–695 (a Tribute to Fausto Calderazzo on the Occasion of his 80th Birthday).
[6] J.A.M. Van Beek, G. Van Koten, W.J.J. Smeets, A.L. Spek, Model for the initial stage in the oxidative addition of I2 to organoplatinum(II) compounds. X-ray structure of square-pyramidal $[Pt^{II}IC_6H_3(CH_2NMe_2)_2\text{-}o,o'(\eta^1-I_2)]$ containing a linear Pt-I-I arrangement, J. Am. Chem. Soc. 108 (16) (1986) 5010–5011.
[7] J.A. van Beek, G. van Koten, G.P. Dekker, E. Wissing, M.C. Zoutberg, C.H. Stam, Synthesis and reactivity towards diiodine of palladium(II) and platinum(II) complexes with non-cyclic and cyclic ligands $\left(C_6H_3\{CH_2NR^1R^2\}_2-2,6\right)$. End-on diiodine-platinum(II) bonding in macrocyclic $[PtI(C_6H_3CH_2NMe(CH_2)_7MeNCH_2-2,6)(\eta^1-I_2)]$, J. Organomet. Chem. 394 (1) (1990) 659–678.
[8] G. van Koten, Novel aspects of η^1-diiodine coordination and diiodine oxidative addition to platinum(II) and halide transfer oxidation reactions of organo-platinum(II) with $Cu^{II}X_2$, Pure Appl. Chem. 62 (6) (1990) 1155–1159.
[9] R.A. Gossage, A.D. Ryabov, A.L. Spek, D.J. Stufkens, J.A.M. van Beek, R. van Eldik, G. van Koten, Models for the initial stages of oxidative addition. Synthesis, characterization, and mechanistic investigation of η^1-I_2 organometallic pincer complexes of platinum. X-ray crystal structures of $[PtI(C_6H_3(CH_2NMe_2)_2-2,6)(\eta^1-I_2)]$ and exo-meso-$[Pt(\eta^1-I_3)(\eta^1-I_2)(C_6H_3CH_2N(t-Bu)Me_2-2,6)]$, J. Am. Chem. Soc. 121 (11) (1999) 2488–2497.
[10] F.A. Cotton, E.V. Dikarev, M.A. Petrukhina, Coordinated and clathrated molecular diiodine in $[Rh_2(O_2CCF_3)_4I_2]\cdot I_2$, Angew. Chem. Int. Ed. Engl. 39 (13) (2000) 2362–2364.
[11] A.Y. Rogachev, R. Hoffmann, Iodine (I2) as a janus-faced ligand in organometallics, J. Am. Chem. Soc. 135 (8) (2013) 3262–3275.
[12] R. Makiura, I. Nagasawa, N. Kimura, S. Ishimaru, H. Kitagawa, R. Ikeda, An unusual six-co-ordinate platinum(II) complex containing a neutral I2 ligand, Chem. Commun. (2001) 1642–1643.
[13] D.M. Ivanov, A.S. Novikov, I.V. Ananyev, Y.V. Kirina, V.Y. Kukushkin, Halogen bonding between metal centers and halocarbons, Chem. Commun. 52 (2016) 5565–5568.
[14] B. Lu, X. Zhang, L.P. Meng, Y.L. Zeng, The Pt (II)···Cl interactions: nature and strength, Chem. Select 1 (18) (2016) 5698–5705.
[15] M. Gao, Q. Li, H.-B. Li, W. Li, J. Cheng, How do organic gold compounds and organic halogen molecules interact? Comparison with hydrogen bonds, RSC Adv. 5 (2015) 12488–12497.
[16] Q. Zhao, The X···Au interactions in the CF3X (X = Cl, Br) ··· Au_n (n = 2, 3, and 4) complexes, J. Mol. Model. 20 (3) (2014) 2133.
[17] J.F. Rooms, A.V. Wilson, I. Harvey, A.J. Bridgeman, N.A. Young, Mercury-fluorine interactions: a matrix isolation investigation of Hg··· F2, HgF2 and HgF4 in argon matrices, Phys. Chem. Chem. Phys. 10 (2008) 4594–4605.
[18] I. Blakey, Z. Merican, L. Rintoul, Y.-M. Chuang, K.S. Jack, A.S. Micallef, Interactions of iodoperfluorobenzene compounds with gold nanoparticles, Phys. Chem. Chem. Phys. 14 (2012) 3604–3611.
[19] Z. Konkoli, D. Cremer, A new way of analyzing vibrational spectra I. Derivation of adiabatic internal modes, Int. J. Quant. Chem. 67 (1998) 1–11.
[20] W. Zou, R. Kalescky, E. Kraka, D. Cremer, Relating normal vibrational modes to local vibrational modes with the help of an adiabatic connection scheme, J. Chem. Phys. 137 (2012) 084114.
[21] W. Zou, D. Cremer, Properties of local vibrational modes: the infrared intensity, Theor. Chem. Acc. 133 (2014) 1451.
[22] W. Zou, D. Cremer, C_2 in a box: determining its intrinsic bond strength for the $X^1\Sigma_g^+$ ground state, Chem. Eur. J. 22 (2016) 4087–4089.
[23] M. Freindorf, E. Kraka, D. Cremer, A comprehensive analysis of hydrogen bond interactions based on local vibrational modes, Int. J. Quantum Chem. 112 (19) (2012) 3174–3187.
[24] K.G. Dyall, Interfacing relativistic and nonrelativistic methods. I. Normalized elimination of the small component in the modified Dirac equation, J. Chem. Phys. 106 (23) (1997) 9618–9626.
[25] W. Zou, M. Filatov, D. Cremer, An improved algorithm for the normalized elimination of the small-component method, Theor. Chem. Acc. 130 (2011) 633–644.
[26] W. Zou, M. Filatov, D. Cremer, Development, implementation, and application of an analytic second derivative formalism for the normalized elimination of the small component method, J. Chem. Theory Comput. 8 (8) (2012) 2617–2629.
[27] D. Cremer, W. Zou, M. Filatov, Dirac-exact relativistic methods: the normalized elimination of the small component method, WIREs Comput. Mol. Sci. 4 (2016) 436–467.
[28] J. Tao, J.P. Perdew, V.N. Staroverov, G.E. Scuseria, Climbing the density functional ladder: nonempirical meta-generalized gradient approximation designed for molecules and solids, Phys. Rev. Lett. 91 (2003) 146401.
[29] K.P. Kepp, Benchmarking density functionals for chemical bonds of gold, J. Phys. Chem. A 121 (9) (2017) 2022–2034.
[30] P. Nava, D. Hagebaum-Reignier, S. Humbel, Bonding of gold with unsaturated species, ChemPhysChem 13 (2012) 2090.
[31] S. Grimme, J. Antony, S. Ehrlich, H. Krieg, A consistent and accurate ab initio parametrization of density functional dispersion correction (DFT-D) for the 94 elements H-Pu, J. Chem. Phys. 132 (15) (2010) 154104.
[32] S. Grimme, S. Ehrlich, L. Goerigk, Effect of the damping function in dispersion corrected density functional theory, J. Comput. Chem. 32 (7) (2011) 1456–1465.
[33] S. Boys, F. Bernardi, The calculation of small molecular interactions by the differences of separate total energies. some procedures with reduced errors, Mol. Phys. 19 (4) (1970) 553–566.
[34] T. Noro, M. Sekiya, T. Koga, Sapporo-(DKH3)-nZP (n = D, T, Q) sets for the sixth period s-, d-, and p-block atoms, Theor. Chem. Acc. 132 (5) (2013) 1363.
[35] T. Noro, M. Sekiya, T. Koga, Segmented contracted basis sets for atoms H through Xe: sapporo-(DK)-nZP sets (n = D, T, Q), Theor. Chem. Acc. 131 (2) (2012) 1124.
[36] T. Noro, M. Sekiya, T. Koga, Correlating basis sets for the H atom and the alkali-metal atoms from Li to Rb, Theor. Chem. Acc. 109 (2) (2003) 85–90.
[37] D. Cremer, J. Grafenstein, T. Koga, Efficient dft integrations by locally augmented radial grids, J. Chem. Phys. 127 (2) (2007) 164113.
[38] D. Cremer, J.A. Larsson, E. Kraka, New developments in the analysis of vibrational spectra: on the use of adiabatic internal vibrational modes, in: C. Parkanyi (Ed.), Theoretical and Computational Chemistry, Theoretical Organic Chemistry, vol. 5, Elsevier, Amsterdam, 1998, pp. 259–327.
[39] R. Kalescky, E. Kraka, D. Cremer, Identification of the strongest bonds in chemistry, J. Phys. Chem. A 117 (2013) 8981–8995.
[40] E. Kraka, J.A. Larsson, D. Cremer, Generalization of the badger rule based on the use of adiabatic vibrational modes in vibrational modes in computational IR spectroscopy, in: J. Grunenberg (Ed.), Computational Spectroscopy: Methods, Experiments and Applications, Wiley, New York, 2010, pp. 105–149.
[41] D. Cremer, E. Kraka, A description of the chemical bond in terms of local properties of electron density and energy, Croat. Chem. Acta 57 (6) (1984) 1259–1281.
[42] D. Cremer, E. Kraka, Chemical bonds without bonding electron density – does the difference electron density analysis suffice for a description of the chemical bond?, Agnew Chem. Int. Ed. Engl. 23 (1984) 627–628.
[43] F. Weinhold, C.R. Landis, Valency and Bonding: A Natural Bond Orbital Donor-Acceptor Perspective, Cambridge Uuniversity Press, Cambridge, UK, 2003.
[44] E. Kraka, W. Zou, M. Filatov, J. Grafenstein, D. Izotov, J. Gauss, Y. He, A. Wu, Z. Konkoli, V. Polo, L. Olsson, Z. He, D. Cremer, COLOGNE2016, see <http://www.smu.edu/catco>, 2014.
[45] E.D. Glendening, C.R. Landis, F. Weinhold, NBO 6.0: natural bond orbital analysis program, J. Comput. Chem. 34 (16) (2013) 1429–1437, http://dx.doi.org/10.1002/jcc.23266.

[46] T. Lu, F. Chen, Multiwfn: a multifunctional wavefunction analyzer, J. Comput. Chem. 33 (2012) 580–592.
[47] M.J. Frisch, G.W. Trucks, H.B. Schlegel, G.E. Scuseria, M.A. Robb, J.R. Cheeseman, G. Scalmani, V. Barone, B. Mennucci, G.A. Petersson, et al., Gaussian 09 Revision A. 1, Gaussian Inc., Wallingford, CT, 2010.
[48] W.W. Porterfield, Inorganic Chemistry, A Unified Approach, Academic Press, San Diego, 1993.
[49] S.M. Huber, E. Jimenez-Izal, J.M. Ugalde, I. Infante, Unexpected trends in halogen-bond based noncovalent adducts, Chem. Commun. 48 (2012) 7708–7710.
[50] K. Szalewicz, Symmetry-adapted perturbation theory of intermolecular forces, WIREs Comput. Mol. Sci. 2 (2) (2012) 254–272.